Reactive Oxygen Species Formation and Peroxide and Carbonyl Decomposition in Aqueous Photolysis of Secondary Organic Aerosols

Lena Gerritz[1#], Jinlai Wei[1#], Ting Fang[1,2], Cynthia Wong[1], Alexandra L. Klodt[1], Sergey A. Nizkorodov[1,*], Manabu Shiraiwa[1,*]

[1] Department of Chemistry, University of California, Irvine, CA, 92697-2025, USA

[2]Sustainable Energy and Environment Thrust, The Hong Kong University of Science and Technology (Guangzhou), Nansha, Guangzhou, Guangdong, 511400, China.

# Equal contribution

# Equal contribution

* nizkorod@uci.edu;* m.shiraiwa@uci.edu

Summary

This supporting information section contains 15 supporting figures and 2 supporting tables, as well as additional information on mass spectrometry operating parameters, spectral flux density for irradiation set up, EPR spectra for SOA and model compounds, mass spectra for α-pinene SOA, SOA photolysis precursor identification and photolysis pathways.

Table of Contents

Liquid-Chromatography interfaced with Mass Spectrometry Specifications

UPLC separation was carried out on a Phenomenex Luna Omega Polar C18 column, 150 × 2.1 mm, with 1.6 μm particles and 100 Å pores, with the temperature set to 30 °C at a flow rate of 0.3 mL min^{-1}. The mobile phase consisted of water (eluent A) and acetonitrile (eluent B), each containing 0.1% formic acid. The gradient elution was programmed as follows: 0−3 min 95% eluent A; 3−14 min linear ramp to 95% eluent B; 14−16 min hold at 95% eluent B; 16−22 min return to 95% eluent A. The MS was operated at a mass resolving power of 1.4×10^5 in a positive/negative ion mode with operating parameters listed in Table S1.

Table S1: Mass Spectrometer Operating Conditions

Parameter	**Positive Ion Mode**	**Negative Ion Mode**
Spray Voltage (kV)	4.0	2.5
Capillary Temperature (C)	80.00	325.00
Sheath Gas	35.00	50.00
Aux Gas	10.00	10.00
Spare Gas	8.00	1.00
Max Spray Current	100.00	100.00
Probe Heater Temperature (C)	200.00	300.00
S-Lens RF level	10.00	30.00

Characterization of spectral flux density

The spectral flux of the EPR *in-situ* irradiation system was characterized using a StellarNet radiometer. The TUV model (https://www.acom.ucar.edu/Models/TUV/Interactive_TUV/) was used to obtain Los Angeles summer solstice maximum and the 24-hour average Los Angeles solar

flux for comparison. The following parameters were used in the TUV calculator: latitude/longitude: 34°/-118°; date and time: June 30, 2021 – data from each hour in the day were acquired and averaged to obtain a 24-hour average spectral flux density or 19:00:00 GMT representing the summer solstice maximum; overhead ozone column: 300 du; surface albedo: 0.1; ground altitude: 0 km; measured altitude: 0 km; clouds optical depth/base/top: 0.00/4.00/5.00; aerosols optical depth/S-S albedo/alpha: 0.235/0.990/1.000; sunlight direct beam/diffuse down/diffuse up: 1.0/1.0/1.0.

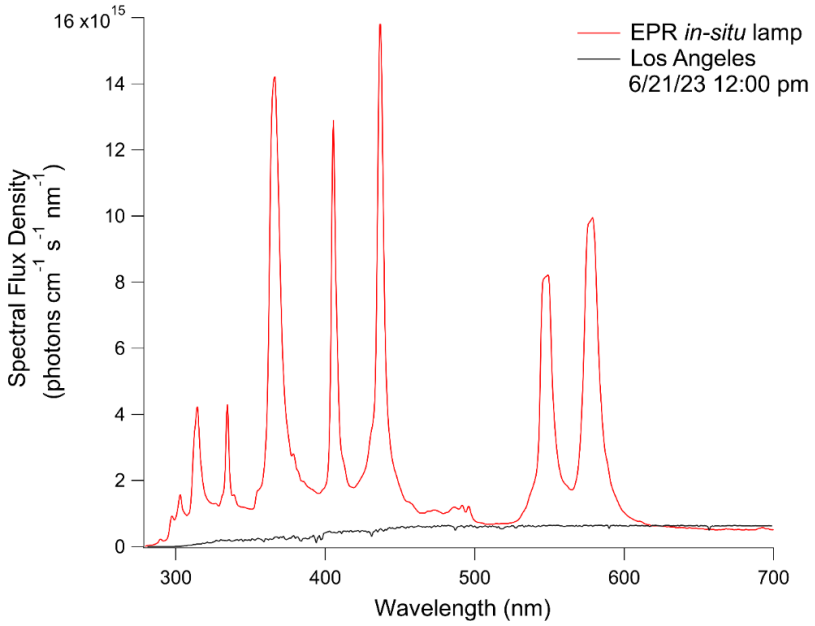

Figure S1. Spectral flux density of the 100 W Hg lamp (300 – 600 nm) incident on the EPR sample compared with the Los Angeles summer solstice maximum.

Identification of Photolysis Precursors and Pathway Prediction

Figure S6 and S7 show the difference in the normalized intensity of a given *m/z* between the dark and irradiated samples for negative and positive ion mode, respectively. The dark and irradiated samples were prepared from the same SOA extract; therefore, the only difference in their mass spectra can be attributed to photochemical aging. For this reason, the four peaks in negative ion mode with the largest absolute decrease after irradiation were analyzed in more

detail to predict the radical products trapped by BMPO. Only C-10 molecules were considered for this analysis as smaller molecules could be artifacts of ion source fragmentation (e.g., via loss of CO_2 or CO),[47] which appeared to be more prevalent in positive ion mode. Only one abundant C-10 precursor was identified in positive ion mode that was not already present in the negative ion mode data, resulting in 5 total compounds selected for fragmentation analysis. The radical photolysis products were predicted by drawing out the Norrish type I and peroxide fragmentation pathways for selected precursors using the most likely structures corresponding to the observed formulas proposed in previous literature.[48,49] All other photolysis pathways producing closed shell products (such as Norrish type II splitting of carbonyls) were not considered as they would not produce BMPO-radical adducts. After fragmentation, it was assumed that all radical products were immediately trapped by BMPO preventing further fragmentation, while non-radical species could undergo further photochemistry.

Discussion of Oxopinonaldehyde Photolysis Products: $C_8H_{13}O$ and $C_8H_{11}O_2$

BMPO-$C_8H_{13}O$ produces a relatively abundant $[M]^+$ adduct at *m/z* 324.217 and a minor $[M+2H]^+$ adduct at *m/z* 326.223. This radical is not produced by any of the other photolysis pathways detailed in Fig. S8-13, which supports that photolysis is occurring via this pathway. The BMPO-C_2HO_2 adduct is not detected as an $[M]^+$ ion and is detected with low relative abundance at $[M+2H]^+$ at *m/z* 260.149. This radical likely undergoes CO elimination resulting in the BMPO-CHO adduct previously described, which would explain its low abundance, so this photolysis pathway may still be occurring.

The final photolysis pathway proposed for oxopinonaldehyde produces $C_8H_{11}O_2$ and C_2H_3O radicals, both of which are detected as BMPO-adducts via mass spectrometry. The $C_8H_{11}O_2$ radical is detected as an $[M]^+$ adduct at *m/z* 338.196 and an $[M+2H]^+$ adduct at *m/z* 340.212. None

of the other photolysis pathways explored in Figs. S7-12 produces a $C_8H_{11}O_2$ radical, although the peak at *m/z* 340.212 could also correspond to the $[M]^+$ adduct of the $C_8H_{13}O_2$ radical produced via photolysis of compounds 2, 4, and 5 (Fig. S8, 10, and 11). The contributions of $C_8H_{13}O_2$ radicals could explain the order of magnitude increase in relative abundance for *m/z* 340.212 over *m/z* 338.196, but the detection of *m/z* 338.196 supports the presence of this photolysis pathway upon irradiation.

Table S2: Hyperfine splitting constants used for the identification of radicals detected by EPR.

BMPO Adduct	g-factor	HFS 1	HFS 2, (3)
BMPO-OOH1	2.0064 ± 0.0001	13.4 ± 0.1	11.9± 0.3
BMPO-OOH2	2.0064 ± 0.0001	13.4 ± 0.1	9.6 ± 0.1
BMPO-OH1	2.0064 ± 0.0001	13.9 ± 0.1	15.3 ± 0.1, (0.54 ± 0.1)
BMPO-OH2	2.0064 ± 0.0001	13.9± 0.1	12.6 ± 0.1, (0.66 ± 0.1)
BMPO-R1	2.0062 ± 0.0001	14.8 ± 0.1	19.9 ± 0.3
BMPO-R2	2.0062 ± 0.0001	15.2 ± 0.1	21.0 ± 0.3
BMPO-OR1	2.0062 ± 0.0001	14.6 ± 0.1	16.9 ± 0.1
BMPO-OR2	2.0063 ± 0.0001	14.6 ± 0.1	16.9 ± 0.1

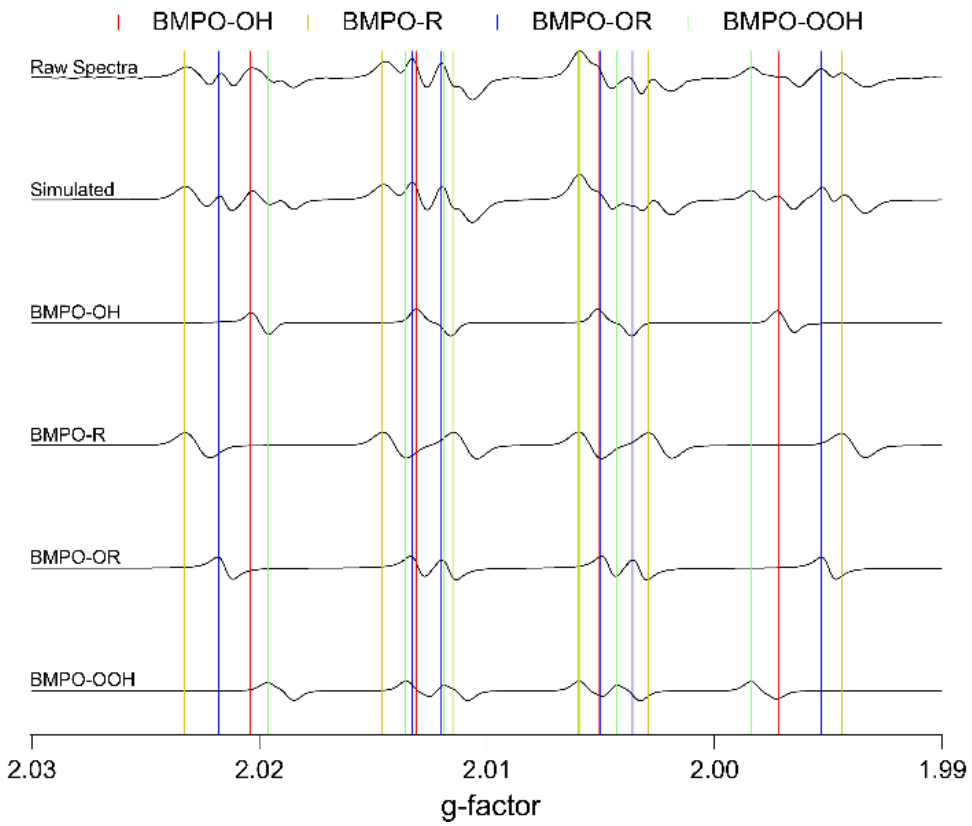

Figure S2. EPR spectra for Isoprene SOA after 10 minutes of irradiation deconvoluted based on radical species.

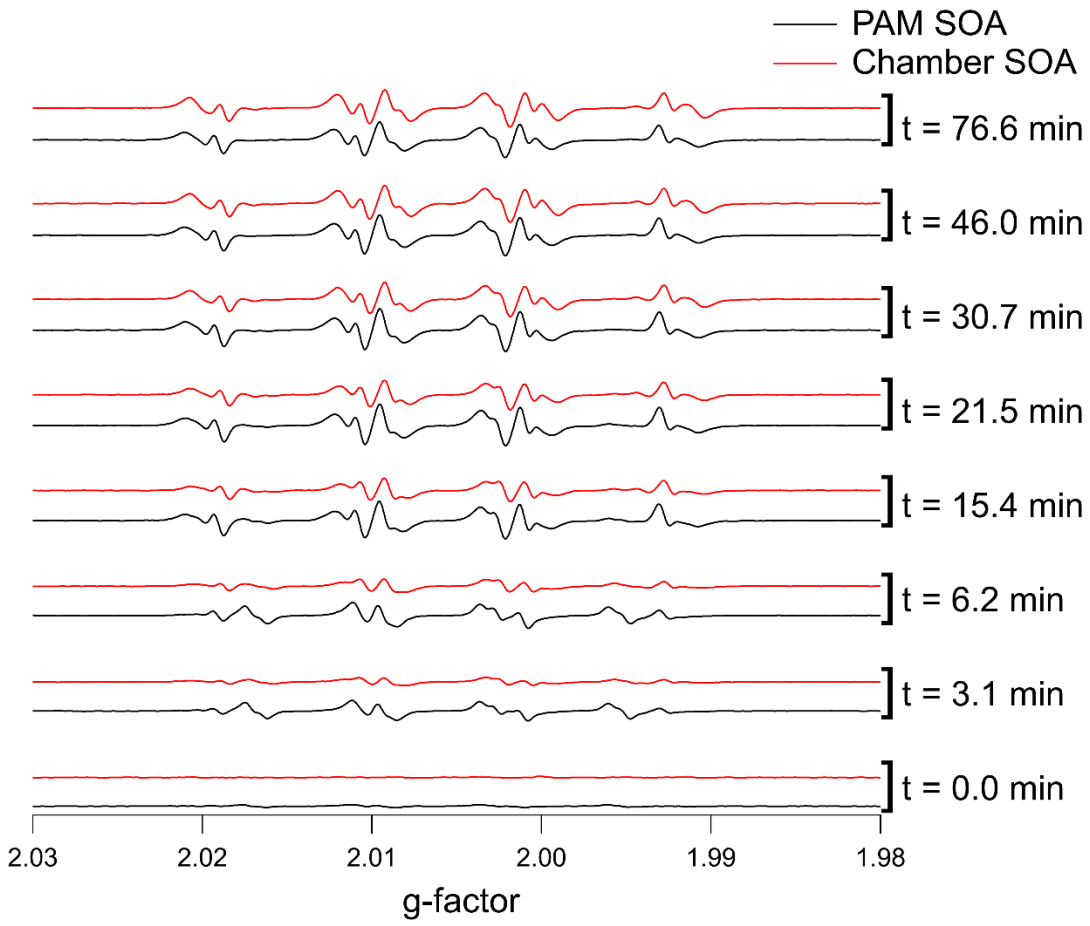

Figure S3. Comparison between EPR spectra over the course of irradiation for water extracts of SOA generated by OH photooxidation of α-pinene in the PAM reactor and the smog chamber.

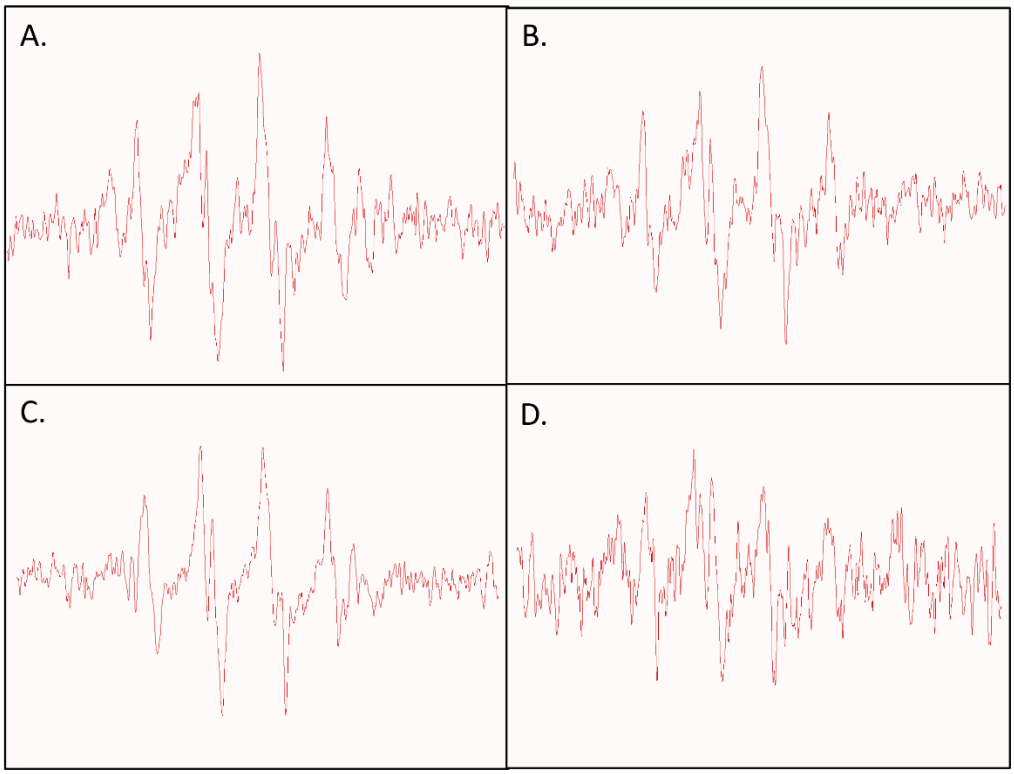

Figure S4. Raw EPR spectra after 75 minutes under dark conditions for A.) isoprene, B.) α-terpineol, C.) α-pinene, and D.) toluene SOA extracts. The majority of the signal can be ascribed to the BMPO-OOH with contributions from BMPO-OH in isoprene SOA (panel A).

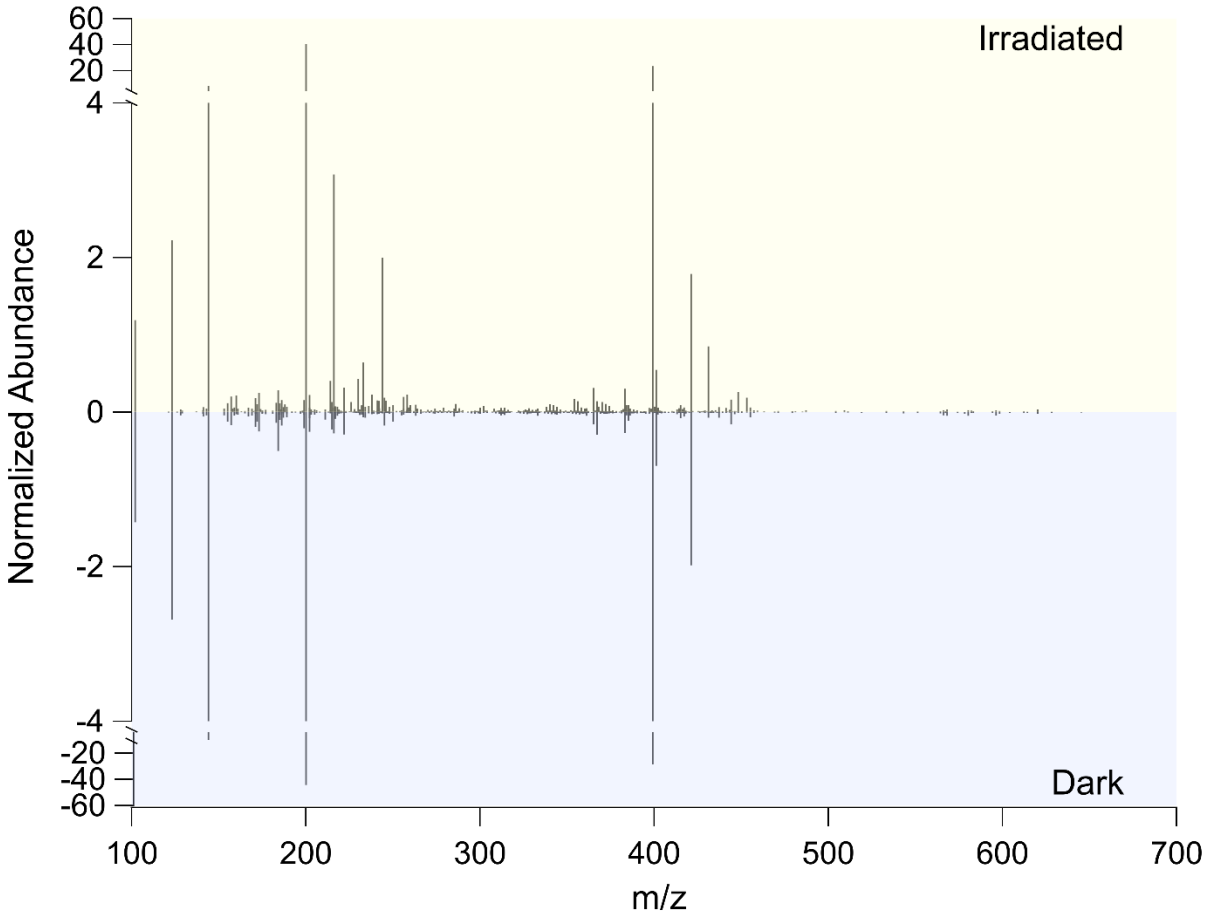

Figure S5. Positive ion mode mass spectra from *m/z* 100-700 of α-pinene SOA extract + BMPO solution before and after irradiation.

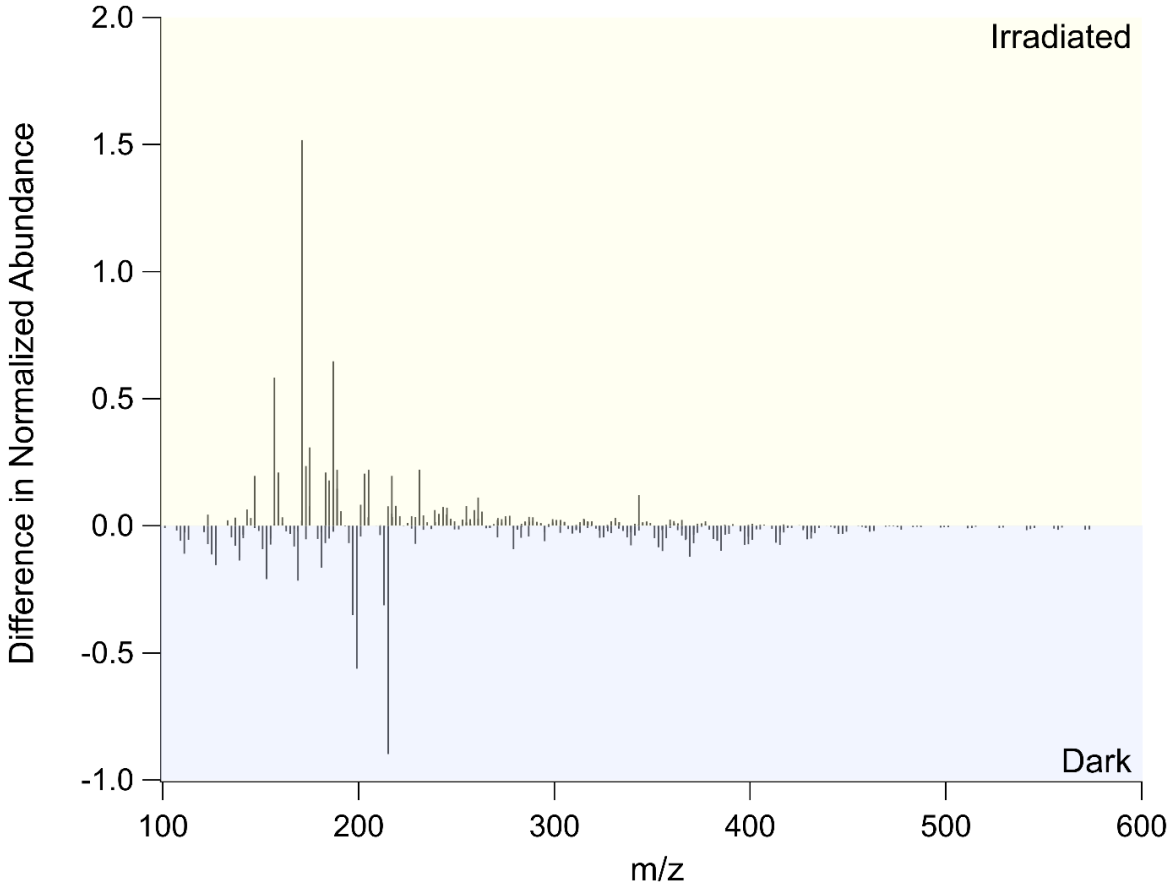

Figure S6. Difference in the normalized relative abundance of the negative ion mode mass spectra before and after irradiation of the α-pinene SOA extract.

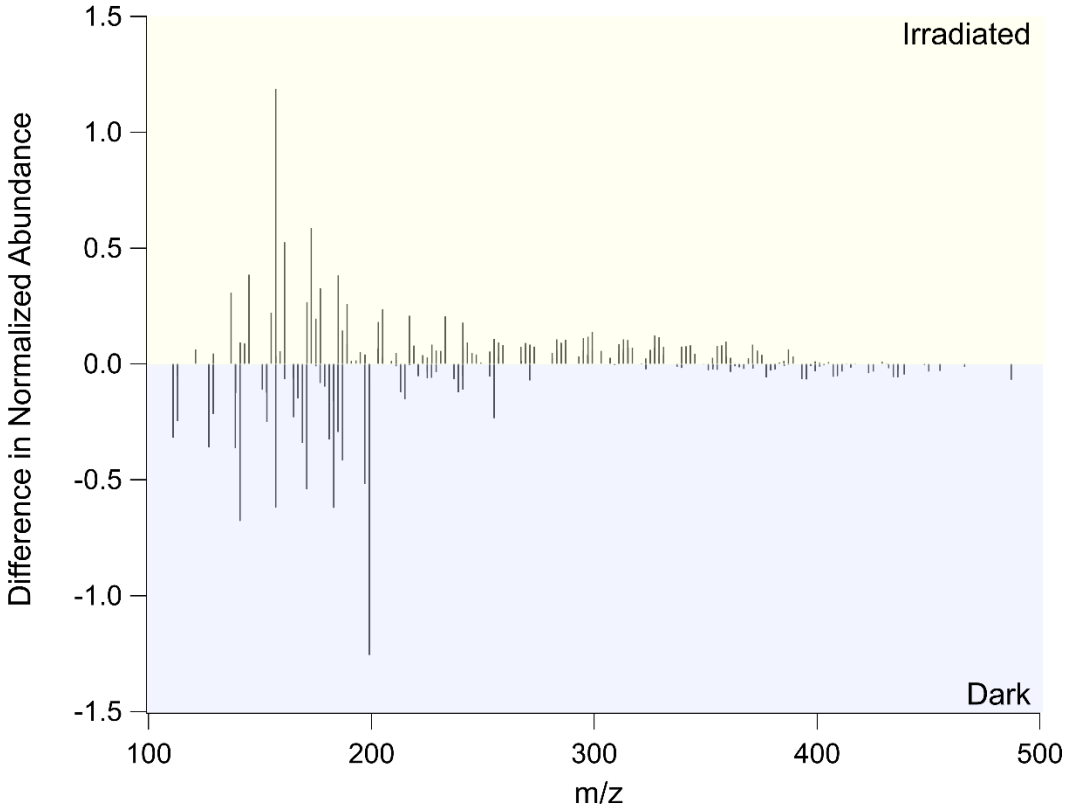

Figure S7. Difference in the normalized relative abundance of the positive ion mode mass spectra before and after irradiation of the α-pinene SOA extract.

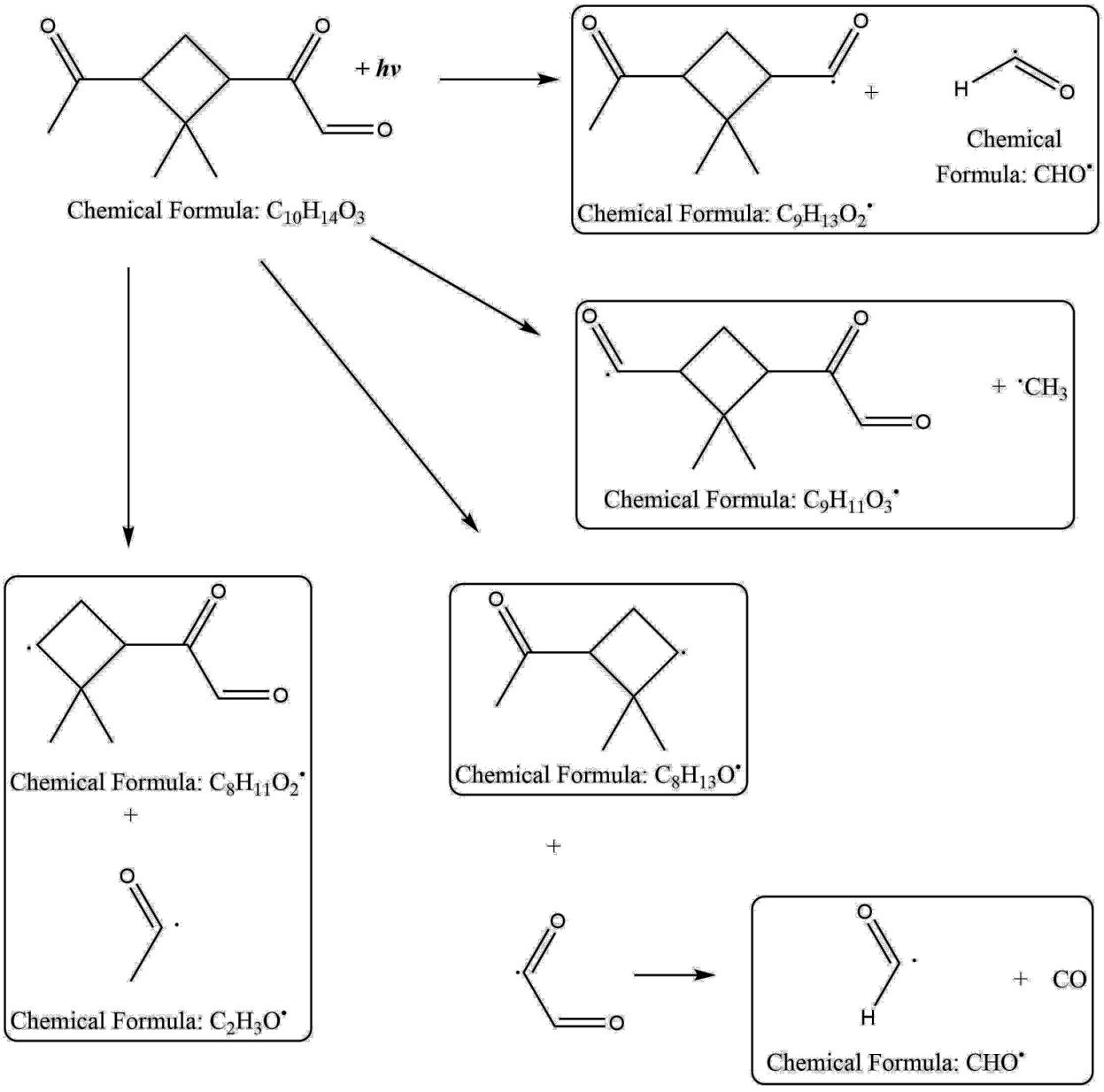

Figure S8. Fragmentation pathways of 2-(3-acetyl-2,2-dimethylcyclobutyl)-2-oxoacetaldehyde (oxopinonaldehyde), compound 1, *m/z* 182

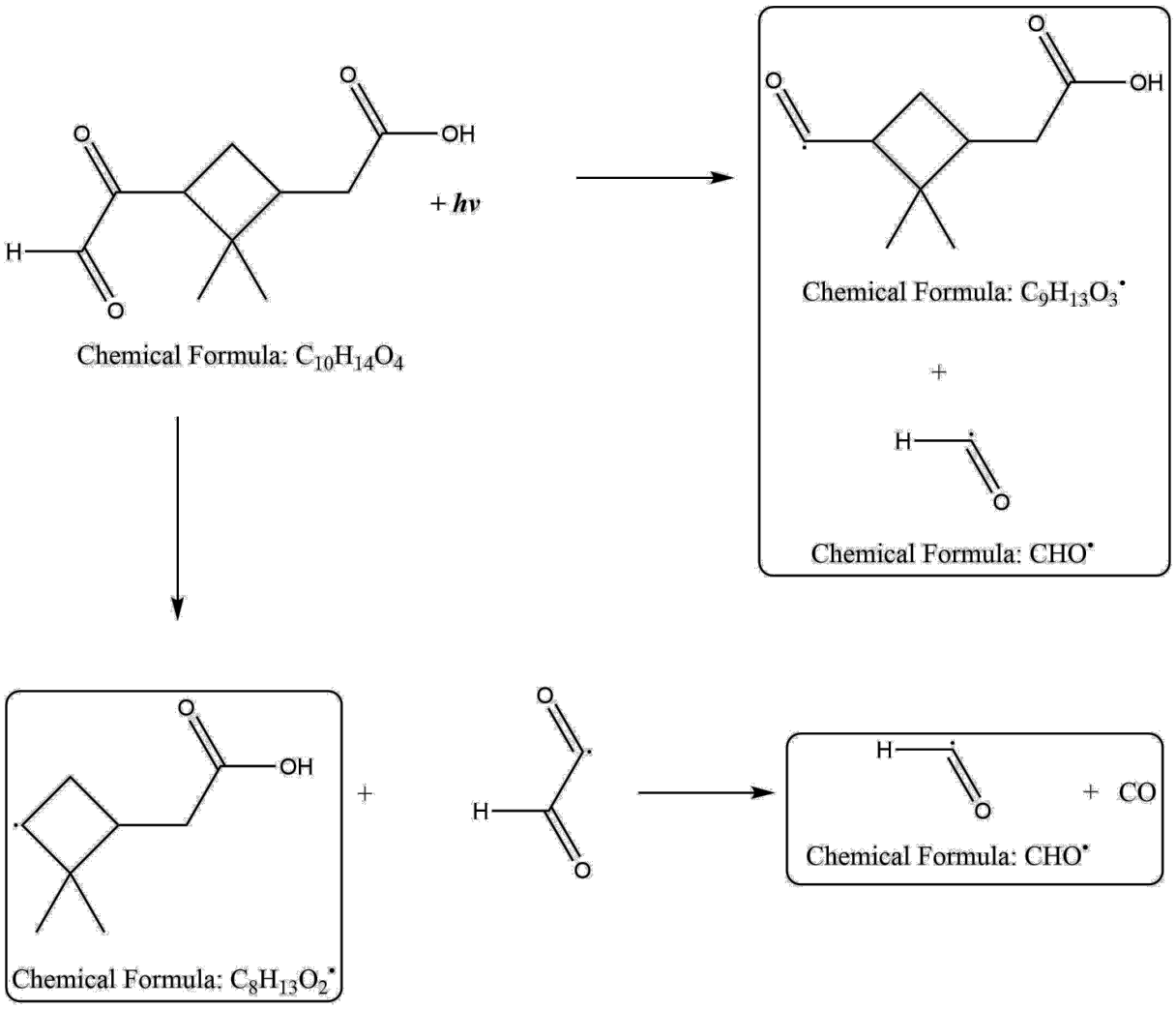

Figure S9. Fragmentation pathways of 2-(2,2-dimethyl-3-(2-oxoacetyl)cyclobutyl)acetic acid (oxopinonic acid), compound 2, *m/z* 198.

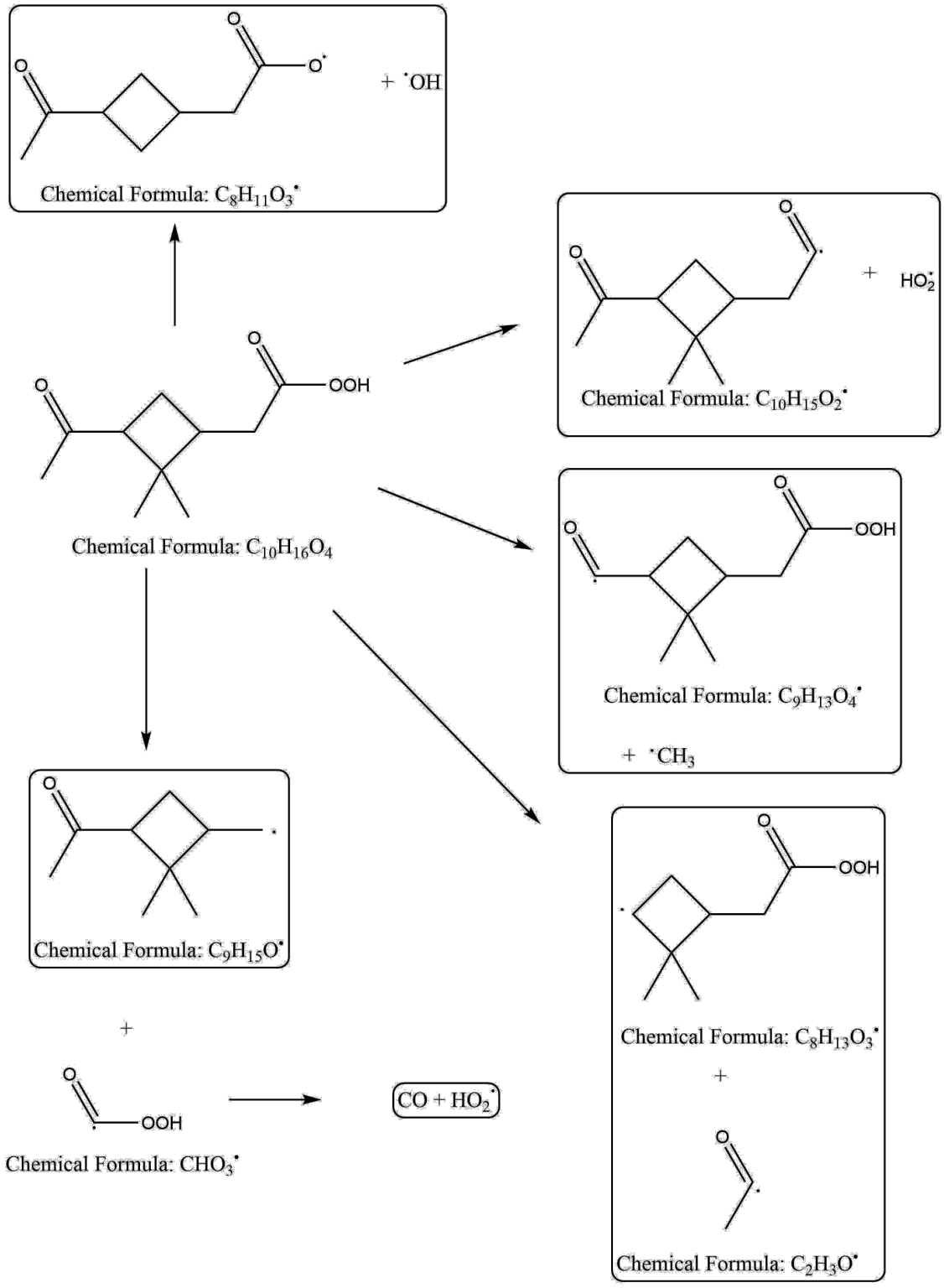

Figure S10. Fragmentation pathways of 2-(3-acetyl-2,2-dimethylcyclobutyl)ethaneperoxoic acid, (peroxy-pinonic acid), compound 3, *m/z* 200.

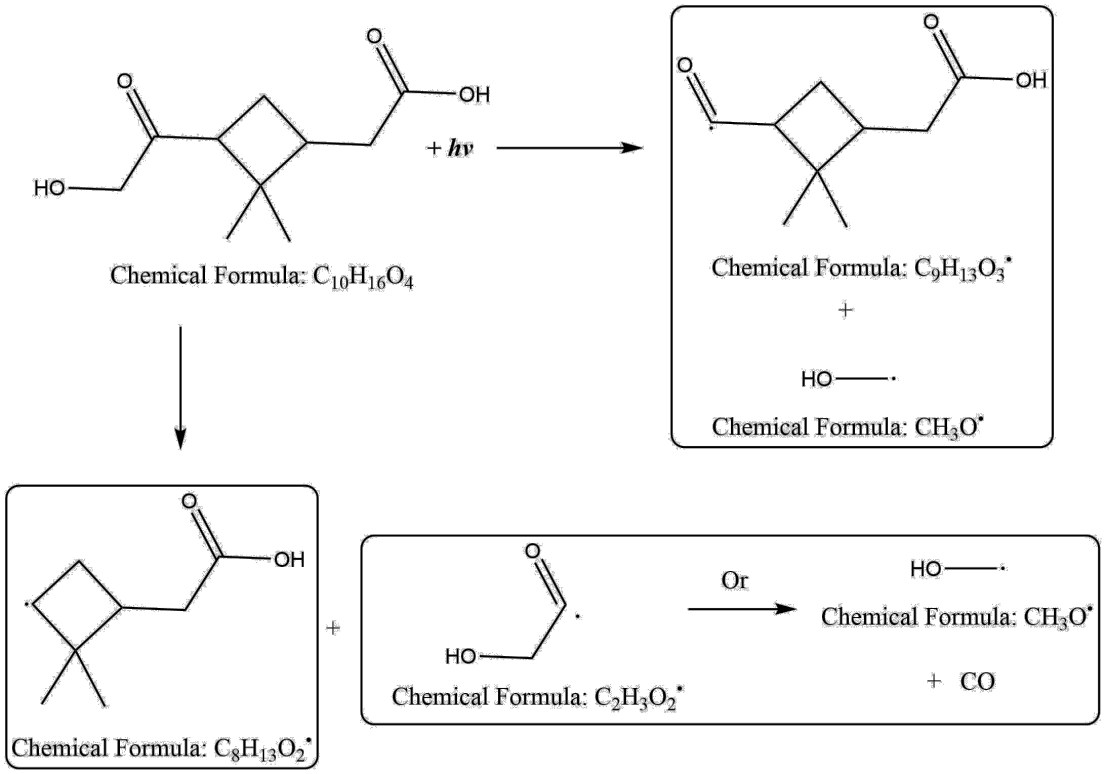

Figure S11. Fragmentation of 2-(3-(2-hydroxyacetyl)-2,2-dimethylcyclobutyl)acetic acid (OH-pinonic acid), compound 4, *m/z* 200.

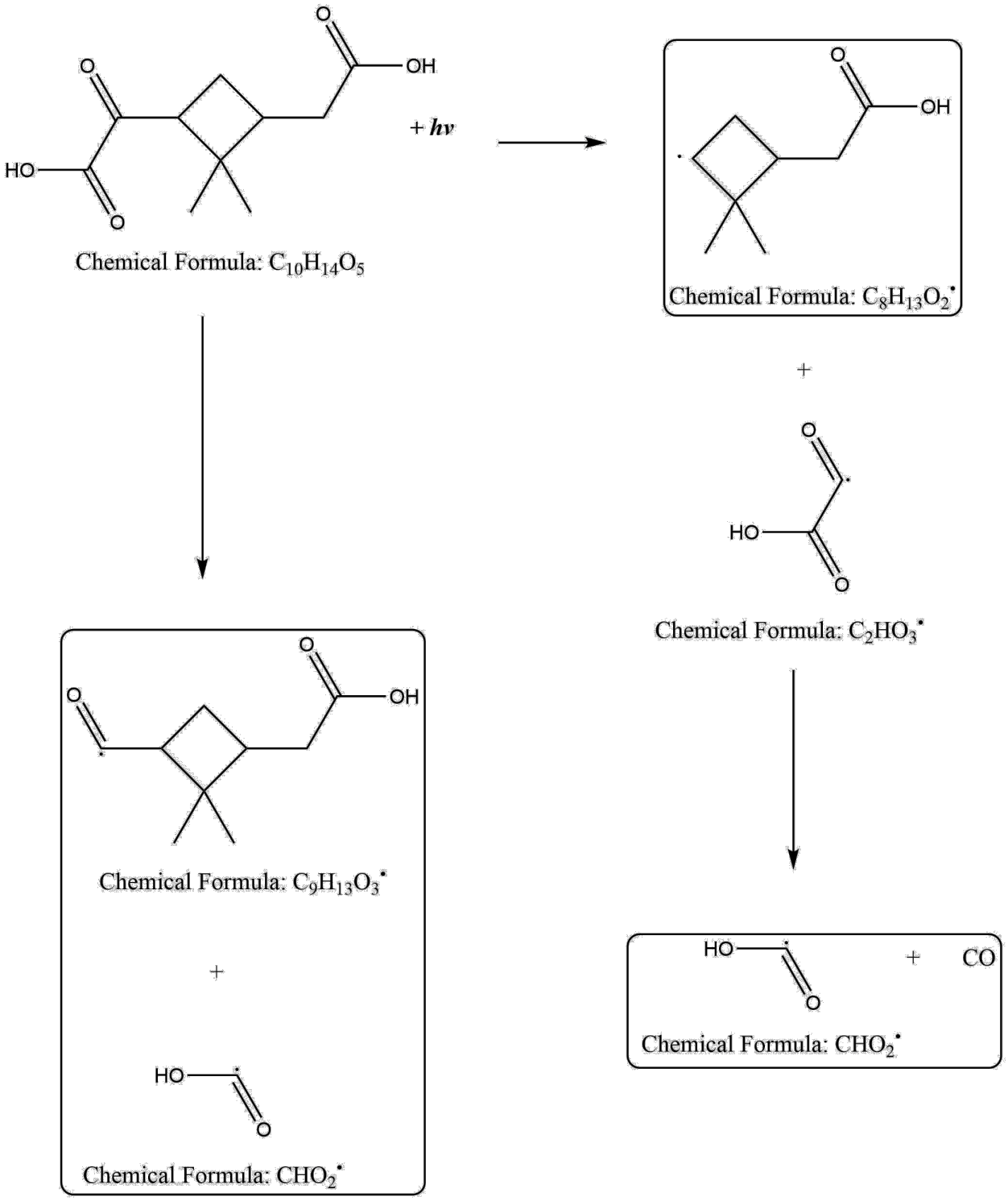

Figure S12. Fragmentation pathways of 2-(3-(carboxymethyl)-2,2-dimethylcyclobutyl)-2-oxoacetic acid (COOH-pinonic acid)), compound 5, *m/z* 214.

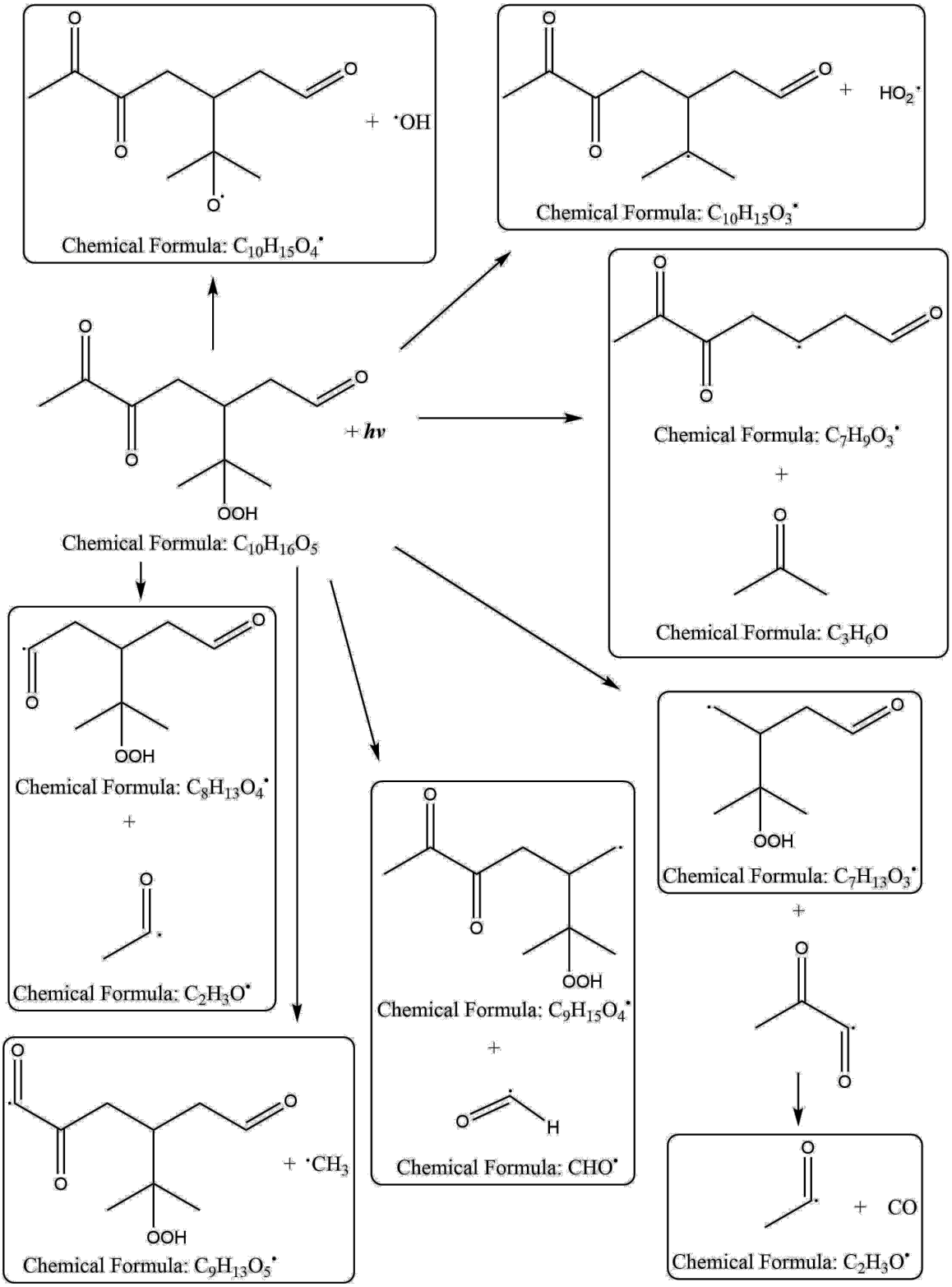

Figure S13. Fragmentation pathways of 3-(2-hydroperoxypropan-2-yl)-5,6-dioxoheptanal, Compound 6, *m/z* 216.

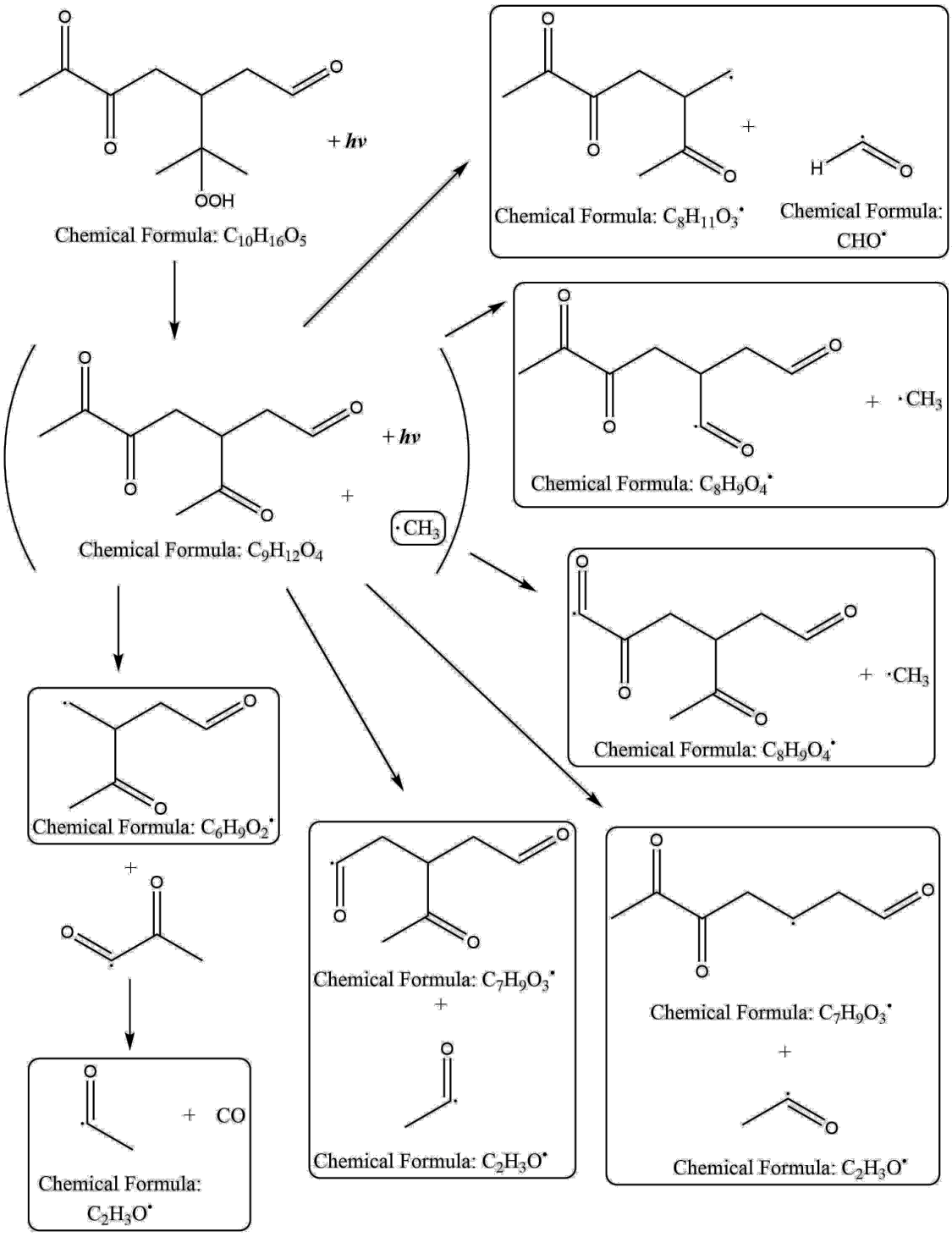

Figure S14. Fragmentation pathways of compound 6a, a photolysis product of compound 6.

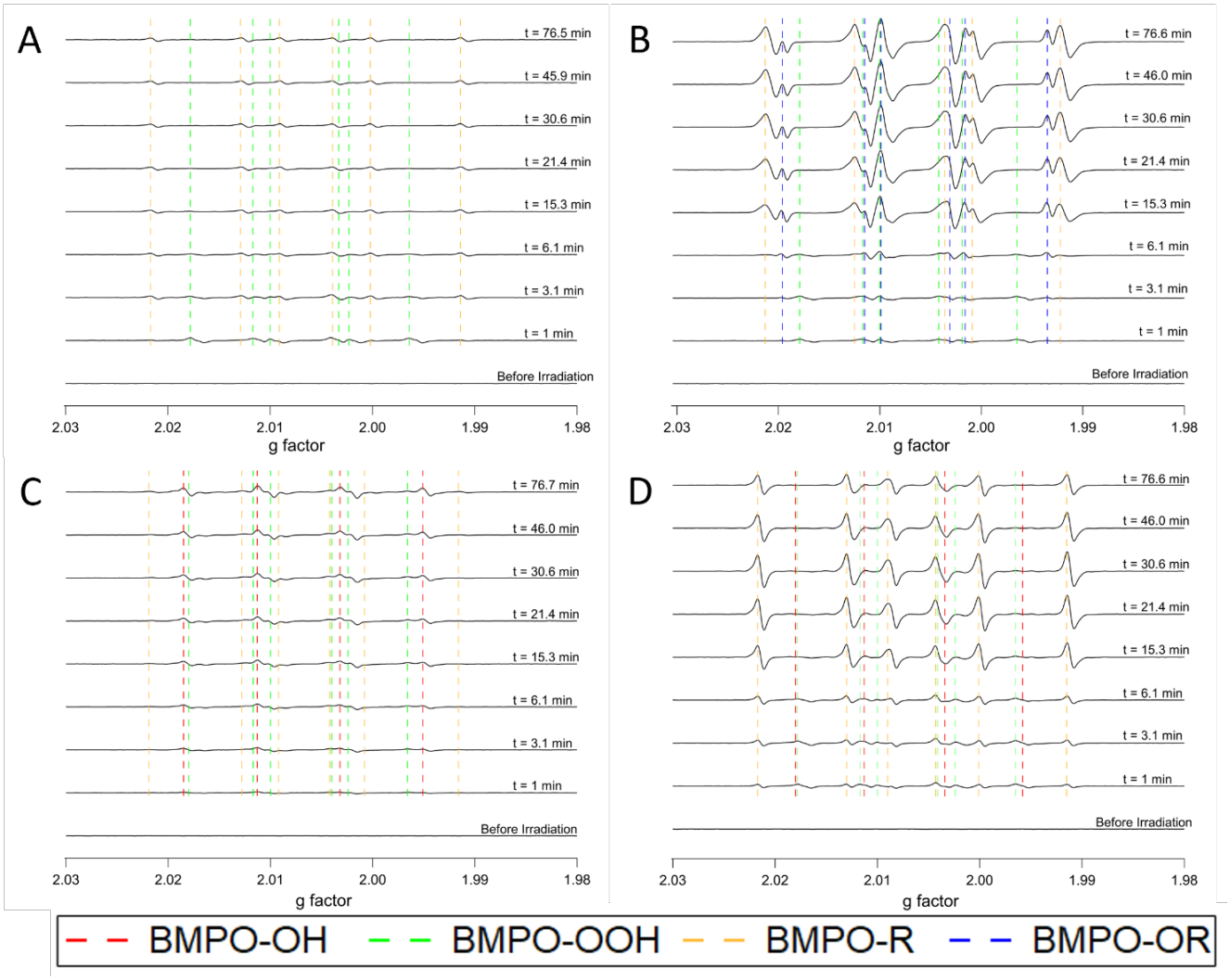

Figure S15. EPR spectra of aqueous solutions of A) cumene hydroperoxide, B) pinonic acid, C) *t*-butyl hydroperoxide, and D) *t*-butyl peroxybenzoate upon photoiradiation for 76 min.